Wetting geometry and deposition patterns manipulation with bi-dispersed particle-laden droplets

Si Xian Lim [a,b], Alistair Guo Hao Teo [b], Kian-Soo Ong [c], Karen Siew Ling Chong [d], Fei Duan [b,*]

[a] Singapore Centre for 3D Printing, Nanyang Technological University, 50 Nanyang Avenue, Singapore, 639798, Singapore
[b] School of Mechanical and Aerospace Engineering, Nanyang Technological University, 50 Nanyang Avenue, Singapore, 639798, Singapore
[c] Institute of Materials Research and Engineering, A*Star, 2 Fusionopolis Way, Innovis, Level 9, Singapore, 138634, Singapore
[d] Institute of Microelectronics, A*Star, 11 Science Park Road, Singapore Science Park II, Singapore, 117685, Singapore

GRAPHICAL ABSTRACT

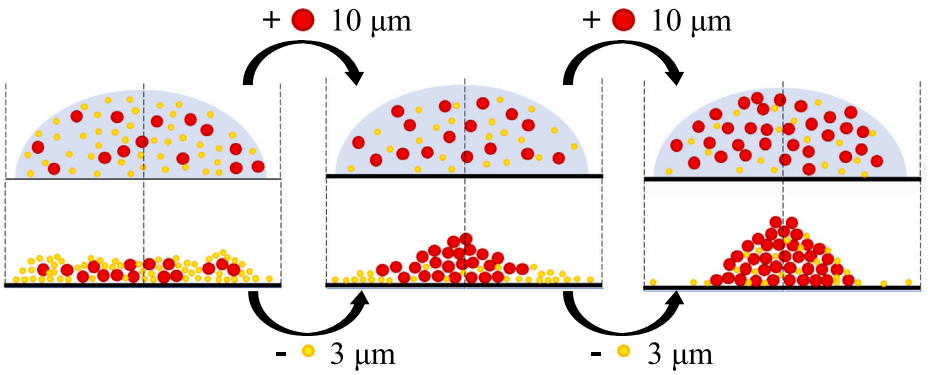

ARTICLE INFO

Keywords:
Particle self-assembly
Bi-dispersed particle-laden droplet
Evaporation
Wetting geometry
Patterned substrate
Polystyrene particles

ABSTRACT

Polygonal deposition through evaporation of the suspension droplets holds promise for printing applications. The distinctive edges present in polygonal droplets offer the potential to enhance printing resolution and enable the fabrication of diverse thin depositions. Prior investigations revolve one dimensional control with the types of wetting geometries and deposition patterns initiate from different driving factors. The current study delves into the synergistic interplay between a bi-dispersed suspension mixing ratio and particle concentration, as they collectively influence the deposition pattern of octagonal droplets formed using a micropyramid cavity patterned substrate. The investigation culminates in the development of a comprehensive phase diagram categorizing four distinct types of deposition: octagonal outer-ring deposition, octagonal ring with irregular features, octagonal uniform deposition, and central deposition. Specifically, octagonal outer-ring deposition is observed when droplets consist predominantly of 3 μm particles at lower concentrations. In cases where a suspension contains 10 μm particles, an intermediate concentration exceeding 50% gives a rise to the octagonal outer-ring deposition intermingled with irregular features. The octagonal uniform deposition emerges when 3 μm particles, co-aggregated with 10 μm particles, are compelled to settle at the deposition center within the mixture at the 3:1 ratio at 1.0 wt% and 2.6 wt%. Notably, the "curvature effect", exhibited by the aggregates adhering to the liquid–air interface, counter-intuitively suppresses octagonal deposition despite the presence of octagonal wetting geometry and forms the central deposition. In summary, the study introduces a robust method to achieve the uniform deposition and proposes a scalable and flexible strategy for generating diverse deposition types through the judicious mixing of two suspension solutions at distinct weight ratios.

* Corresponding author.
E-mail address: feiduan@ntu.edu.sg (F. Duan).

1. Introduction

Droplet-based printing has firmly established itself as a viable technique for creating functional surfaces and coatings in defined areas [1,2]. Consequently, there has been a growing focus among researchers on surface patterning achieved through particle deposition via the evaporation of suspension fluids. The manipulation of various influencing factors enables precise control over droplet evaporation behavior, leading to the formation of distinct deposition patterns [3]. The impact of factors such as solute size and concentration [4,5] on deposit thickness and the coffee-ring width, the role of ambient conditions [6–10] and surfactants [11–13] in inducing Marangoni vortex flow within droplets for particle repositioning, exemplify the complexity of the self-assembly process. The industrial applications benefited from the advancements includes inkjet printing [14–17], coating [18–20], DNA microarrays [21–24], cell micropatterning [25–27], and sensor fabrication [28–30]. Particularly, achieving uniform deposition patterns has emerged as a central objective in numerous studies, owing to its critical significance and applicability [31,32]. The pursuit of uniformity has yielded a multitude of methodologies, encompassing techniques such as incorporating surfactant [33], lowering pH values [34], increasing relative humidity [6], and manipulating particle sizes within solutions [35]. While the past approaches have demonstrated success in achieving uniform deposition, conventional circular patterns exhibit inherent limitations that impede their effectiveness. The limitations manifest in a reduction in printing resolution due to the absence of sharp edges and straight lines along the print outline, and suboptimal packing configurations inherent to circular geometry constraints. Circular deposition patterns fail to deliver the precision of sharp edges and straight lines that are essential for maintaining high printing resolutions. Moreover, the absence of connecting edges necessitates the stacking of multiple droplets to form a circular venn structure, which proves impractical for adequately covering the wetting region. The inherent constraint renders circular deposition ill-suited for the fabrication of thin-layered sensors [36], such as surface-enhanced Raman spectroscopy substrates [37–41] and microelectromechanical systems substrates [42]. In light of these challenges, the concept of polygonal depositions has garnered considerable interest. Polygonal depositions hold the promise of overcoming these geometric limitations, making them a compelling area of exploration and innovation. By enabling the creation of intricate shapes and well-defined edges, polygonal deposition techniques offer a viable solution to the shortcomings posed by circular patterns.

The exploration of polygonal deposition commenced with investigations into the geometric manipulation of water or suspension droplets. Pioneering this endeavor, Vrancken et al. embarked on an experimental and numerical journey and revealed how triangular and diamond-shaped pillars on a patterned substrate dynamically constrain the water contact line, thereby engendering octagonal and inequilateral hexagonal geometries, respectively [43]. A distinct avenue was elucidated by Raj and Kumar, who harnessed the power of micropillar patterned substrates to sculpt water droplets to the shapes of square, rectangular, hexagonal, octagonal, and dodecagonal patterns, by ingeniously modulating pillar spacing and arrangement [44]. Subsequently, Kubyshikina et al. orchestrated the deposition of non-circular and square aluminum oxide nanoparticles using diverse geometrical micropillar-patterned substrates [45]. In addition to utilizing patterned substrates, Iqbal et al. controlled the wetting geometry by crafting substrates with a soft polygonal core. The three-phase contact line of the droplet would depin from the stiffer region and conform towards the softer core design, resulting in triangular, square, or precisely controlled circular depositions [46]. As the field evolved, an increased emphasis on the interplay between geometry and deposition type emerged. Park et al. finessed the spacing of cylindrical micropillars to yield uniform hexagonal deposition, absent of disruptive cracks [47]. Simultaneously, Kim et al. charted a divergent path, manipulating the surface energy of cylindrical micropillar patterns to orchestrate the formation of densely populated hexagonal deposition patterns, harnessing a bi-dispersed suspension comprising 2 μm and 10 μm polystyrene particles [48]. Meanwhile, Pyeon et al. artfully countered the coffee-ring effect by orchestrating confined evaporation-induced Marangoni flows within triangular, square, and hexagonal droplets, culminating in uniform triangle, square, and hexagon quantum dots atop a hybrid wetting surface [49]. Cumulatively, the evolution of polygonal deposition research coalesces around two pivotal fronts: the modification of substrates to manipulate wetting geometry and the influence of external factors to direct deposition patterns. Yet, the paradox lies in the constraints that accompany these advancements. While environment-based controls inherently limit each printing process to a singular deposition type, the utilization of distinct patterned substrates curtails the latitude to effect wetting geometry changes with a single substrate. In response to these limitations, the present manuscript endeavors to unveil a scalable and adaptable methodology primed for integration within diverse applications. The proposed method uniquely empowers the generation of varied deposition patterns through the manipulation of solute effects, thereby transcending the conventional confines and propelling polygonal deposition into new possibilities.

An effective approach to meeting these criteria involves the utilization of either the original suspension solution or their judicious combination. This approach aligns seamlessly with printing processes that often necessitate the withdrawal of multiple solutions, each possessing distinct compositions, to achieve the desired color mixture [50]. The inherent adaptability of the method was substantiated in the earlier research, wherein self-assembly of bi-dispersed particle-laden droplets yielded a versatile spectrum of deposition patterns, ranging from “volcano-like” and “mountain-like” to the intricate “coffee-ring” and the sought-after “uniform” patterns [51–53]. Building upon the insights and motivated by the challenges encountered in prior endeavors, particularly the inability to achieve octagonal uniform deposition at elevated particle concentrations via particle size manipulation [54]. The introduction of a minute quantity of particles, selectively sedimented within a bi-dispersed solution, emerges as a potential strategy to coerce smaller particles into sedimentation upon contact, thereby enhancing deposition uniformity.

In the pursuit of deeper comprehension, an intriguing hypothesis arises: augmenting the larger particle content within the composition could potentially hinder particles from reaching the contact line. The predicted phenomenon, in turn, might trigger a depinning process, effectively eliminating particles from the contact line and consequently resulting in the formation of irregular deposition patterns. Guided by the hypotheses, this study embarks on an investigation to unravel the intricate interplay between the mixing ratio of a bi-dispersed solution and particle concentration. Specifically, our focus is directed toward the formation of octagonal deposition patterns upon a micropyramid cavity patterned substrate.

2. Methods

2.1. Experiments

A comprehensive array of 20 bi-dispersed solutions, each comprising 3 μm and 10 μm polybead microspherical particles from Polyscience Inc., was prepared by varying ratios and concentrations. Each particle size is deposited onto a surface and measured to ensure that the 3 μm and 10 μm particles fall within the range of 3–3.30 μm and 9–11 μm, respectively, as documented in the company brochure. To encapsulate the diverse interplay of variables, the bi-particle size suspension was adeptly combined at three distinct weight ratios: 1:0, 3:1, 1:1, 1:4 and 0:1 for 3 μm:10 μm particles. To ensure pristine experimental conditions, the solutions underwent a purification process, involving successive centrifugation and ultrasonic treatment cycles using the D3024 DragonLab centrifuge and CREST ultrasonic equipment for 10 min each.

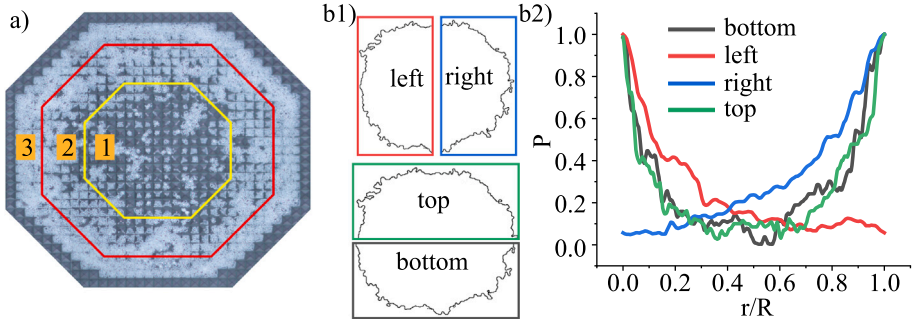

Fig. 1. (a) Partitioning the deposition pattern into three sections as labeled in the figure: The yellow octagon represents partition 1, which is half of the deposition, whereas Partition 2 in the red octagon encompasses an additional 30% of the deposition size from Partition 1. Partition 3 is the region from Partition 2 to the outermost boundary of the deposition. (b1) Slice the irregular outline of the deposition into four different halves, ranging from left, right, bottom, and top. (b2) Extracting the outline of each slice to a normalized profile distance (P) against normalized width (r/R).

The prepared suspensions were subsequently subjected to dilution to achieve concentrations of 0.1 wt%, 0.5 wt%, 1.0 wt%, and 2.6 wt% using Type I deionized water (18 MΩ cm). The preparation was undertaken with utmost care to avert the occurrence of coagulation, thereby preserving the suspension integrity. The diligent preparation of each of the 20 solutions preceded the experimental phase to forestall any unintended deviations or anomalies. The polymethyl methacrylate substrate, is intricately etched with square-based micropyramid cavities, a feat accomplished through precise nano-imprint lithography techniques. The side length of the pyramid base is 30 μm and the depth of the cavity is 11 μm. Further details regarding the specific design of the micropyramid cavity can be found in Ref. [54]. The experimental protocol was set into motion by the controlled deposition of 0.4 μl droplets onto the patterned substrate, executed utilizing the Eppendorf Research Plus micropipette. A choreographed orchestration of observation and documentation followed. The top view of the intricate evaporation processes of the bi-dispersed particle-laden droplets was recorded utilizing the Nikon Eclipse LV100ND Microscope, while the complementary side view was captured with the Hi-Spec Camera. The experimental apparatus found its stable residence atop the Vision IsoStation Optical Workstation, ensconced within an acrylic shield to maintain controlled experimental conditions. The ambient environment for droplet evaporation was maintained at a constant temperature of 22 ± 1 °C and humidity levels of 55 ± 2%. To attain robust and statistically reliable results, each solution underwent three trials of experimentation, yielding comprehensive error bars for all ensuing measurements.

2.2. Analysis methods

The first method, introduced in Fig. 1(a), compares the impact of reverse capillary flow for depositions containing irregular 10 μm particles distributed near the contact line. The first method involves counting the number of 10 μm particles that are visible from the top of the deposition for each partition, as labeled in Fig. 1(a). The first partition bounds half of the octagonal wetting radius, while the second partition encircles an additional 30% increase in the wetting radius, and the third partition expands from 80% to the edge of the deposition.

The Distance to Border (DTB) method sliced the binary outline of the deposition into four different halves, as depicted in Fig. 1(b1) [55]. The profile of each slice is extracted and normalized in the plot, as illustrated in Fig. 1(b2). Subsequently, the profile is subtracted from the profile of the reference polygons to derive an error profile against each polygon. The polygonal representation of the outline can then be determined by computing the Root Mean Square Error (RMSE) from the error profile.

3. Results and discussion

Droplets dispensed onto the micropyramid cavity-patterned substrate were hindered from spreading uniformly in all directions. The square base pyramid structure introduces resistance acting on the contact line, and the resistance varies between the parallel and inclined directions at a 45° angle to the square base. Consequently, the droplets adopt an octagonal wetting geometry. The 20 bi-dispersed solutions of various compositions allowed the suspended particles within the liquid to self-arrange into different configurations as the droplets underwent complete evaporation. Fig. 2 presents a comprehensive phase diagram that delineates the distinct deposition patterns arising from varied particle–particle and liquid–particle interactions. Conclusive insights into each deposition type within different zones are obtained through cross-sectional confocal images, referenced by black dotted arrows. The horizontal axis of Fig. 2 demarcates the vertical regions, effectively categorizing deposition patterns based on diverse mixing weight ratios for 3 μm to 10 μm particles. Meanwhile, the vertical axis serves to illustrate the shifts in deposition patterns concerning particle concentration, with increasing particle concentration from 0.1 wt% to 0.5 wt%, 1.0 wt% and 2.6 wt% from the bottom.

Examining Region (a) in Fig. 2 reveals the presence of octagonal ring deposition, characterized by the predominant accumulation of particles around the periphery of the three-phase contact line. Notably, for suspension droplets of 0.1 wt% at the weight ratios of 3:1 and 1:1, singular octagonal ring patterns manifest (refer to Fig. 2(a1,a3)). While both respective droplets experience depinning as the evaporation process progresses, the distinctive interaction stemming from the bi-particle sizes ensures the 3 μm particles anchor within the recessed cavity. The resultant deposition pattern stands in stark contrast to the irregular rings observed with the pure colloidal of 3 μm particles in Fig. 1(f1). Transitioning to Region (b) of Fig. 2, an even distribution in deposition becomes apparent at the weight ratio of 1:4 and 0:1 at 0.1 wt% particle concentration.

Leica DMC8 confocal microscope is used to obtain the particle distribution profile from the center of the deposition as illustrated in the legend of Fig. 3. The particle distribution plot arranged in the sequence of increasing the 10 μm particle within the mixture from top to bottom, with green plot for the single colloid of 3 μm particle, red plot for the bi-dispersed solution at the weight ratio 3:1, blue plot for the bi-dispersed solution at the weight ratio 1:1, yellow plot for the bi-dispersed solution at the weight ratio 1:4, and orange plot for the pure colloidal of 10 μm particle. From Fig. 3(a), an unobtrusive trend can be observed when the weight ratio of 10 μm particle in the mixture increases at the lowest concentration of 0.1 wt%, particles accumulate near the contact line shift towards the center. A more evident reduction of particles accumulated at both ends and the increase of particles deposited in the center of the deposition can be seen for the particle

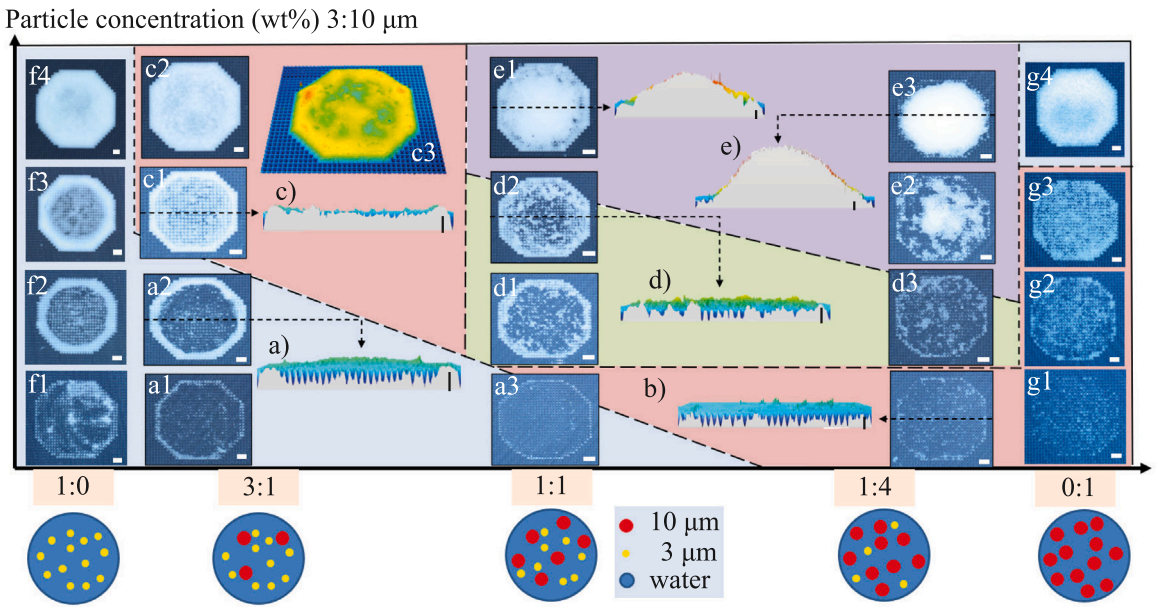

Fig. 2. A phase diagram categorizing distinct deposition patterns is presented in Fig. 2. (a) Octagonal outer-ring depositions are shown, forming with suspension droplets at a weight ratio of 3:1 for (a1) 0.1 wt%, (a2) 0.5 wt%, and at a weight ratio of 1:1 for (a3) 0.1 wt%. A cross-section confocal image depicting the octagonal outer-ring deposition is extracted from (a2). (b) A cross-section confocal image and top view portray uniformly distributed particles originating from a suspension droplet at a weight ratio of 1:4 and 0.1 wt%. (c) showcases uniform deposition patterns generated by suspension droplets at a weight ratio of 3:1 for (c1) 1.0 wt% and (c2) 2.6 wt%. A cross-section confocal image of the uniform deposition is derived from (c1), while a three-dimensional (3D) confocal image of (c2) is depicted in (c3). (d) Octagonal outer-ring depositions with irregular bits are captured, emerging from suspension droplets at (d1) 0.5 wt% and (d2) 1.0 wt% for a weight ratio of 1:1, and at (d3) 0.5 wt% for a weight ratio of 1:4. A cross-section confocal image capturing the octagonal outer-ring deposition with irregular bits is extracted from (d2). (e) displays central depositions with cross-section confocal images in (e1) and (e3). (e1) showcases a central deposition on an octagonal platform stemming from a suspension droplet at a weight ratio of 1:1 and 2.6 wt%. Central depositions are formed by suspension droplets at a weight ratio of 1:4 for (e2) 1.0 wt% and (e3) 2.6 wt%. The black scale bar in all cross-section confocal image represent 11 μm. (f) Deposition patterns formed with pure colloidal containing 3 μm for (f1) 0.1 wt%, (f2) 0.5 wt%, (f3) 1.0 wt%, and (f4) 2.6 wt%. (g) Deposition patterns formed with pure colloidal containing 10 μm for (g1) 0.1 wt%, (g2) 0.5 wt%, (g3) 1.0 wt%, and (g4) 2.6 wt%.Scale bar in all images represent 100 μm.

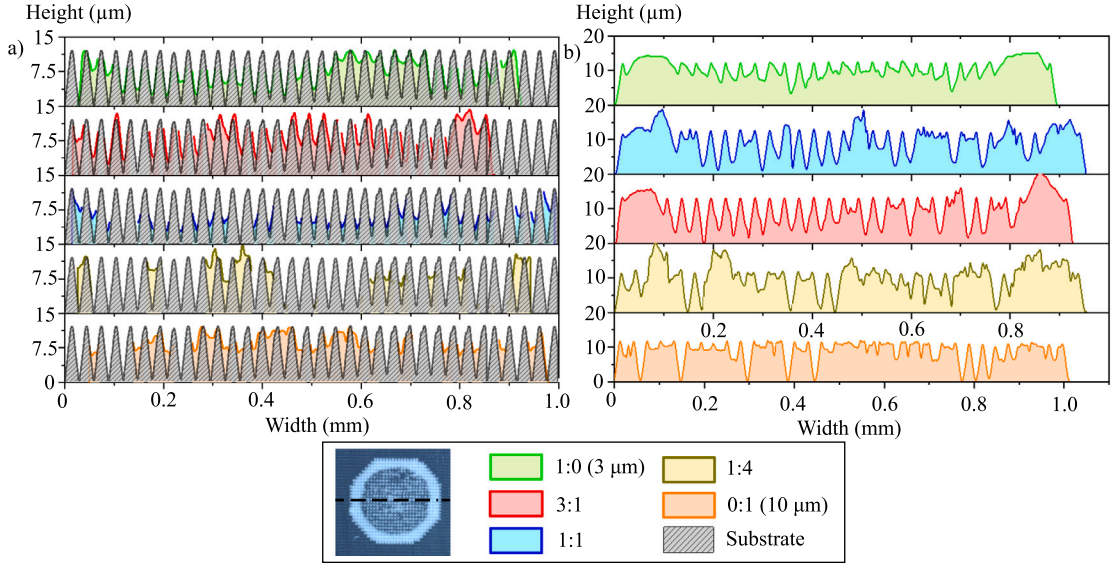

Fig. 3. Confocal microscopy data extracted horizontally across the center of the deposition patterns. (a) Comparing the particle distribution for 0.1 wt% from top to bottom in the following sequence, 1:0, 3:1, 1:1, 1:4, and 0:1 in terms of weight ratio. Micropyramid cavity patterned microstructures are colored in gray as the particles available in the lowest concentration are unable to fill above the cavity. (b) Comparing the particle distribution for 0.5 wt% from top to bottom in the following sequence, 1:0, 3:1, 1:1, 1:4, and 0:1 in terms of weight ratio.

concentration at 0.5 wt% as pictured in Fig. 3(b). As particle concentration escalates to 0.5 wt% at the weight ratio of 3:1, an octagonal outer-ring deposition akin to the mono-dispersed 3 μm particle-laden drop at identical particle concentration is observable as illustrated in Fig. 2(a2,f2). At the same particle concentration at 0.5 wt%, similar octagonal ring patterns persist in the bi-dispersed droplet of the weight ratio 1:1 and 1:4 as pictured in Fig. 2(d1,d3) but not with the pure colloid of 10 μm in Fig. 2(g2).

In Region (c), the deposition patterns formed at the weight ratio 3:1 engender uniform deposition, illustrated vividly in Fig. 2(c). Cross-sectional confocal images in Fig. 2(c1) and a 3D confocal depiction in Fig. 2(c3) corroborate the pronounced uniformity captured in

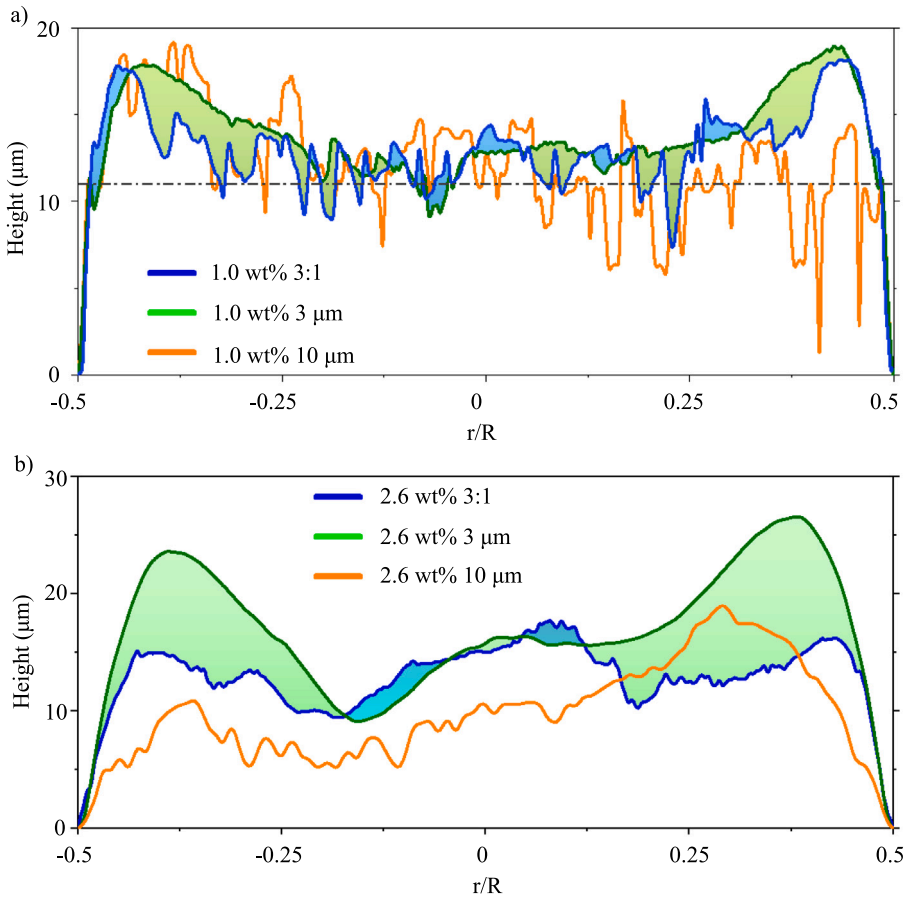

Fig. 4. (a) Confocal microscopy data comparing the particle distribution among single colloidal droplets containing 3 μm (green) and 10 μm (orange) particles, and a bi-particle suspension droplet at a mixing ratio of 3:1 (blue), at 1.0 wt% with normalized width, r/R. Dash dotted line represent the height of the micropyramid cavity structure. (b) Confocal microscopy data comparing particle distribution among single colloidal droplets containing 3 μm (green) and 10 μm (orange) particles, and a bi-particle suspension droplet at a mixing ratio of 3:1 (blue), at 2.6 wt% with normalized width, r/R above the micropyramid cavity structure. The green-colored region indicates where the green plot surpasses the blue plot, while the blue-colored region denotes where the blue plot surpasses the green plot.

Fig. 2(c2). The pivotal factor of critical sedimentation radius emerges, with the 10 μm particles surpassing the threshold, prompting their descent toward the substrate [56]. The propensity of the 10 μm particles to aggregate with the 3 μm particles, thereby triggering direct sedimentation. The outcome of the bi-particle interactions is a heightened concentration of deposits centralized within the wetting geometry core. Concurrently, the remaining unaggregated 3 μm particles are swept toward the contact line courtesy of capillary outward flow. Fig. 4 compares the particle distribution of pure colloids consisting of the 3 μm and 10 μm particles against the deposition of a bi-particle system with the weight ratio of 3:1 along a normalized wetting radius. The dash-dotted line in Fig. 4(a) represents the height of the cavity structure while Fig. 4(b) merely encapsulates the deposition above the cavity structures. In the figure, the particle distribution for the 10 μm particles reflects the irregular distribution of particles on both ends due to the liquid–air interface adsorption as discussed in Ref. [54]. Hence, the depositions formed at the weight ratio 3:1 at 1.0 wt% and 2.6 wt% are compared against the 3 μm particle deposition. In Fig. 4, the distribution height for the deposition at the weight ratio 3:1 higher than the 3 μm are colored in blue, and green contrariwise. The plot in Fig. 4 both illustrates a higher and wider outer-ring distribution near the contact line with lesser particles residing at the drop center in the 3 μm colloidal deposition.

Subsequently, as the weight ratio of 10 μm particles within the composition increased to 50% and beyond, a distinctive shift was observed. Specifically, octagonal outer-ring deposition accompanied by irregular bits emerged within the deposition patterns in the 0.5 wt% and 1.0 wt% deposition at the weight ratio of 1:1, as well as at the 0.5 wt% deposition with the weight ratio of 1:4 (refer to Fig. 2(d)). The intriguing facet of the irregular bits, situated at the deposit center, finds its origin in the aggregation of both the 3 μm and 10 μm particles. A distinctive lining of the 10 μm particles in proximity to the contact line, as meticulously highlighted in Fig. 5(a). The scattered island-like bits encircling the contact line are attributed to the reverse capillary action, a phenomenon elucidated in the work of Weon et al. [57]. The intricacies of particle dynamics within bi-dispersed solutions prove pivotal. The propensity of smaller particles to preferentially locate themselves at the three-phase contact line merits attention due to the predilection rooted in the smaller particles proclivity to be transported via the capillary outward flow. The smaller particles could nimbly navigate through the interstitial spaces formed between larger particles and the contact line. Consequently, a spatial separation is instigated, whereby the larger particles are strategically positioned at a distance from the contact line. The spatial disparity triggers a distinctive geometric configuration, where particles coming into contact with the liquid–air interface adopt a wedge-like form pictorial in Fig. 5(b). The particle arrangement prompts the surface tension force stemming from the liquid–air interface to converge toward the center of the droplet, creating a pronounced reverse capillary action. The liquid–air interface exerts a force that effectively repels larger particles away from the contact line, heralding particle size segregation [46,53,57]. Illustrative insights into the reverse capillary action are vividly evident in Fig. 5(c1,c2). The interplay unfolds as the aggregates, characterized by the red, yellow, and blue circles, initially approach the contact line before retracing their path backward. The culmination of this

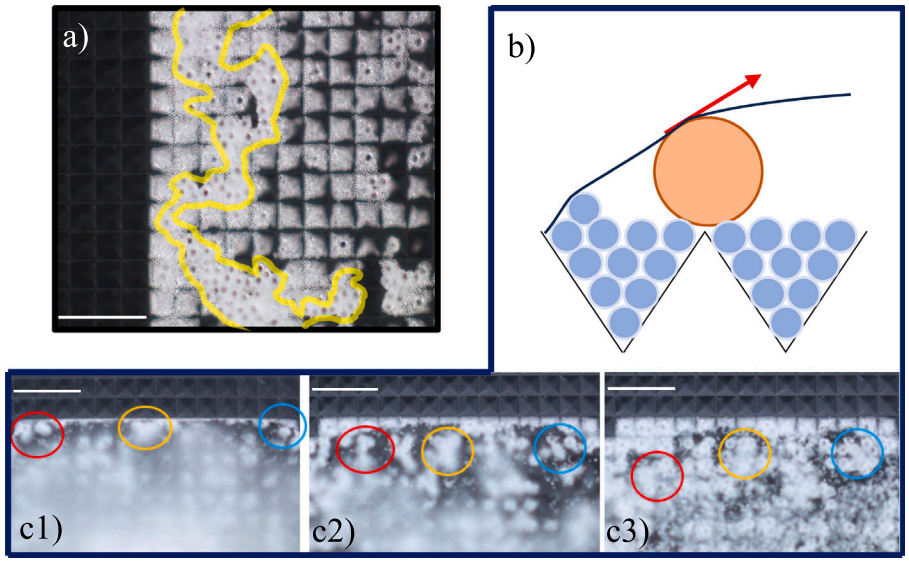

Fig. 5. (a) Magnified view on the contact line of the 1.0 wt% deposition of weight ratio 1:1, the yellow lines depicts the irregular lining of the 10 μm particles deposited adjacent to the contact line. (b) The reverse capillary action on the larger particles by the surface tension force of the liquid–air interface. (c1) illustrates the point at which three aggregates of 10 μm particles in a suspension droplet at a weight ratio of 1:1 and 1.0 wt% approach the three-phase contact line. (c2) depicts the movement of the 10 μm particle aggregates away from the three-phase contact line as the droplet undergoes evaporation. Subsequently, in panel (c3), the aggregates combine with nearby clusters and are deposited in proximity to the three-phase contact line. Across all images, white color scale bars indicate a scale of 100 μm.

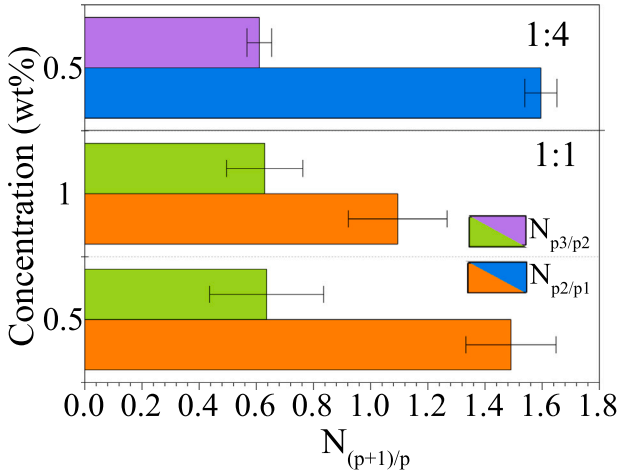

Fig. 6. The ratio of the 10 μm particles visible from the top of the octagonal ring with irregular bits is compared between the ascending partitions at different particle concentrations. $N_{p2/p1}$ compares the number of 10 μm particles between the second and the first partition, with an orange horizontal bar representing deposition with the weight ratio of 1:1 and a blue horizontal bar for the weight ratio of 1:4. $N_{p3/p2}$ compares the number of 10 μm particles between the third and the second partition, with a green bar for deposition with the weight ratio of 1:1 and a purple bar for the weight ratio of 1:4.

intricate dance materializes in Fig. 5(c3), wherein the aggregates amalgamate with other 10 μm particle clusters, ultimately depositing near the contact line.

The reverse capillary action primarily affects the 10 μm particles that come into contact with the liquid–air interface near the three-phase contact line. A method to characterize the impact of reverse capillary action on the deposition pattern is devised by counting the 10 μm particles that are visible from the top of the deposition patterns and computing their ratio, $N_{(p+1)/p}$, for each partition. The $N_{p3/p2}$, shown in purple and green in Fig. 6, demonstrates a similar average and is considerably below unity, confirming the consistency of the size segregation effect in pushing the 10 μm particles away from the contact line. The size segregation effect on the $N_{p3/p2}$ ratio shows varying error widths but similar averages, regardless of particle concentration and mixing weight ratio. Given the low $N_{p3/p2}$ and high $N_{p2/p1}$, it can be inferred that most particles are trapped within the second partition, which is neither in the outer ring nor in the center of the deposition.

Moving to the final region depicted in Fig. 2(e), a central deposition becomes evident in bi-dispersed droplets featuring the 1:1 ratio at 2.6 wt%, and the 1:4 ratio at both 1.0 wt% and 2.6 wt%. A nuanced distinction between these two weight ratios is vividly illustrated in the cross-sectional confocal image of Fig. 2(e). At the weight ratio of 1:1 and 2.6 wt%, the deposition takes on a central form atop an octagonal base. In contrast, the central deposition seen at the 1:4 ratio, particularly at 1.0 wt% and 2.6 wt%, manifests in an irregular configuration and a more orderly central disposition, respectively. The intriguing dynamics at play during the droplet evaporation process are rendered comprehensible through Fig. 7(a) and Supporting Video SV1, where the droplet with the weight ratio of 1:4 at 1.0 wt% and 2.6 wt% demonstrates a distinct flocculation process that draws dispersed clusters together as the droplet gradually evaporates. Remarkably, The flocculation was not observed with the pure colloidal of the 10 μm particles, which are typically drawn towards the contact line at 2.6 wt% [54]. A noteworthy distinction emerges in the case of bi-particle size aggregates. The aggregates exhibit a distinct behavior, hovering at a consistent height within the liquid–air interface, yet the droplet drying kinetics prevent the full convergence of clusters towards the droplet center, leading to the irregular central deposition. However, the expected particle size segregation phenomenon is absent due to the discrepancy in the structural intricacies surrounding the three-phase contact line. Specifically, the 3 μm particles fail to fill the microstructure cavities around the contact line adequately, a key prerequisite for the formation of a wedge-like geometry between the larger particle aggregates and the liquid–air interface. Two primary interactions can be attributed to the phenomenon of central deposition, aptly elucidated through the schematic diagram in Fig. 8(a). The first pertains to particle–particle packing dynamics within the bi-dispersed solution, while the second is anchored in the forces exerted on particles adsorbed at the liquid–air interface. The diagram captures the trajectory of aggregate diffusion towards the drop apex, alongside the outward flow of un-aggregated smaller particles towards the contact line due to the capillary flow. The kinetic energy disparity between the smaller and larger particles, attributed to Brownian motion [58–60], underscores

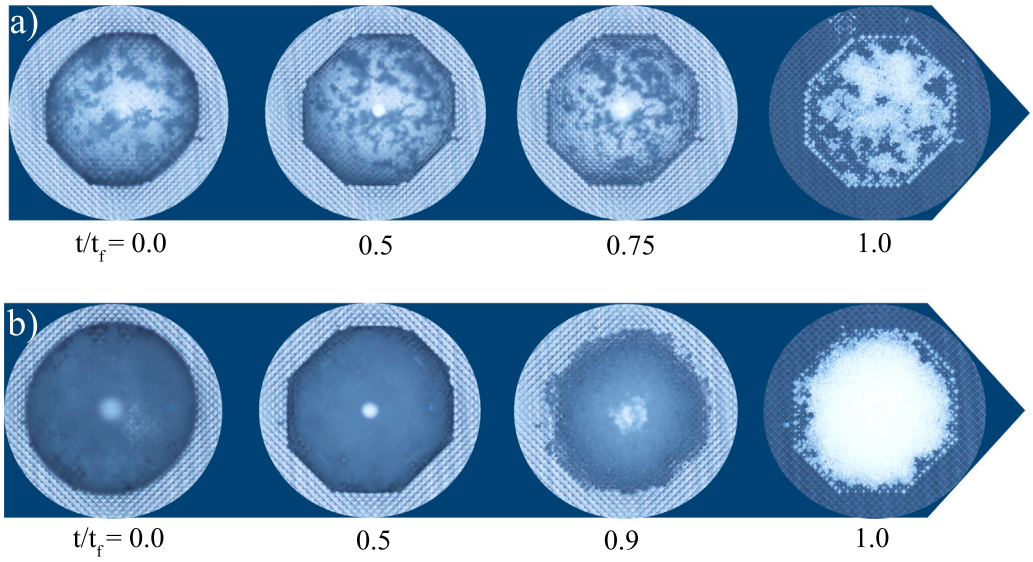

Fig. 7. (a) Different evaporation stages of the particle-laden droplet with weight ratio 1:4 at 1.0 wt%. (b) Different evaporation stages of the particle-laden droplet with weight ratio 1:4 at 2.6 wt%. t_f is the full droplet lifetime.

the first interaction. Within a suspension largely composed of the 10 μm particles, the smaller particles substantially enhance particle–particle collisions and interactions with clusters. Moreover, the ability of the 3 μm particles to effectively envelop each 10 μm particle lends itself to a bridging effect, where the 3 μm particles emerge as binders that facilitate the agglomeration of neighboring clusters. The intricate configuration is absent in pure colloidal solutions due to the spherical geometry of particles, which precludes the close packing and diminishes the potential for such interactions. The second interaction stems from the behavior of larger particles absorbed within the liquid–air interface layer. In the high concentration scenarios, these particles are often unable to sediment due to the dominance of surface tension forces over their weight [61]. As the particles lack close-packing potential, they accumulate as a single layer within the interface. In contrast, the bi-dispersed solutions that favor close packing foster the formation of larger clusters adsorbed within the interface layer. The resulting aggregates amplify both the volume and buoyant force of the clusters. With the surface tension forces at the liquid–air interface prevailing over the weight of the 10 μm particles, a buoyancy-driven flocculation process ensues, driving particle aggregates toward the droplet apex. Figs. 7(b) and 8(b2,b3) elucidate the absence of the 3 μm particles pinning the contact line, ultimately leading to the depinning of the three-phase contact line and the resultant central deposition. Contrastingly, Fig. 8(c2,c3) unveils the contact line being firmly pinned in place by a substantial number of 3 μm particles. Additionally, the side profile image in Fig. 8(c1) obtained from the Hi-Spec camera highlights a deformity within the liquid–air interface layer, stemming from the concurrent pinning of the contact line and aggregation of particles at the droplet apex. The culmination of the dynamics yields a central deposition, distinctly situated atop an octagonal platform constituted predominantly of 3 μm particles.

The confocal microscopy images in Fig. 9 correspond to the two different halves of the particle distribution of the two central depositions described in Fig. 8. The green plot on the left illustrates the central deposition of the weight ratio 1:1 being roughly half the height of the central deposition formed at weight ratio 1:4. The central deposition on octagonal platform had a similar deposition height just above the micropyramid cavity structure from wetting radius 0.35 to 0.45 mm. Contrary to the deposition at weight 1:1, the confocal image on the right side of Fig. 9 underscores a central deposition that lacks octagonal features, despite the predominant octagonal wetting geometry observed throughout most of the droplet evaporation process. The resulting

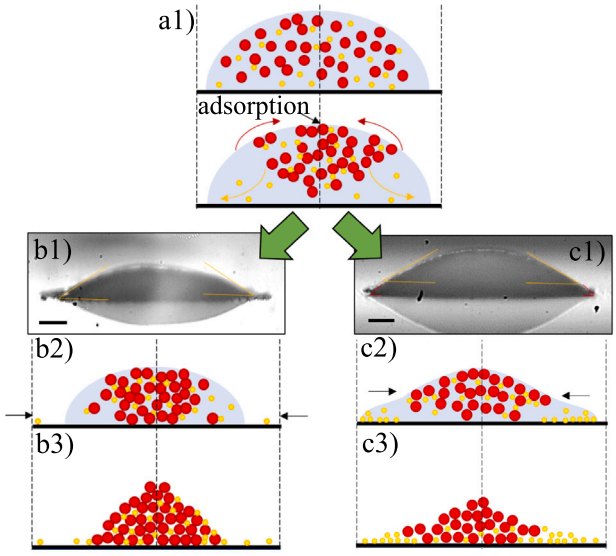

Fig. 8. (a) presents a schematic diagram elucidating the phenomenon where liquid–air interface adsorption propels the aggregates of 10 μm particles towards the droplet's apex, while the smaller 3 μm particles are conveyed towards the contact line via capillary outward flow. (b1) A schematic side profile depicts the characteristics of a 2.6 wt% 1:4 particle-laden droplet. (b2) The depinning of the contact line leaves faint trails of 3 μm particles along the initial wetting periphery, while the remaining particles assemble in a (b3) central deposition pattern. (c1) A schematic side profile outlines the behavior of a 2.6 wt% 1:1 particle-laden droplet. (c2) The droplet apex accumulates particles and the smaller particle pins the contact line concurrently, causing a deformation of the liquid–air interface. (c3) Central deposition surrounds by 3 μm particles.

deposition pattern referred to as the curvature effect, is marked by the deposition inheriting its geometry from the particle locations. The aggregates ensnared within the liquid–air interface acquire a circular geometry from the hemispherical cap, leading to a central deposition characterized by a rather circular outline. The hydrophobicity of the substrate plays a crucial role in determining the available spherical cap surface area for the curvature effect to take hold.

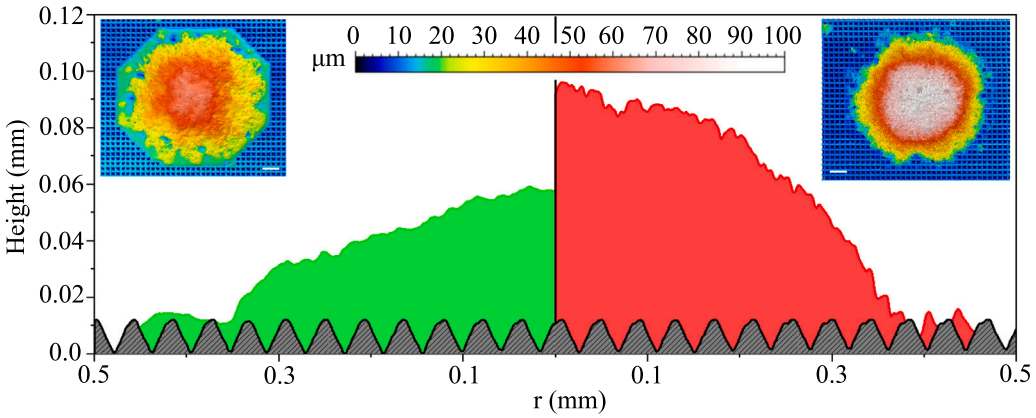

Fig. 9. 3D confocal image of the resulting central deposition, formed by a suspension droplet at the mixing ratio of 1:1 (green) and 1:4 (red) at 2.6 wt%. The rainbow color scale bar signifies the height within the confocal images, spanning from 0 to 100 μm.

Table 1
RSME of the plot profile difference (ΔP) extracted using DTB method on the bi-dispersed mixture of 1:1 at 2.6 wt% against the reference octagon [55].

	RSME (ΔP)					
	Circular	Triangle	Pentagon	Hexagon	Heptagon	Octagon
Bottom	0.0760	0.1290	0.1508	0.1292	0.0570	0.0447
Left	0.0769	0.3743	0.1847	0.1652	0.1353	0.0361
Right	0.0942	0.3367	0.1455	0.1243	0.0989	0.0258
Top	0.1093	0.6310	0.2491	0.1454	0.1705	0.0186
Average	0.089	0.3678	0.1825	0.1410	0.1161	0.0313

Table 2
RSME of the plot profile difference (ΔP) extracted using DTB method on the bi-dispersed mixture of 1:4 at 2.6 wt% against the reference polygons [55].

	RSME (ΔP)					
	Circular	Triangle	Pentagon	Hexagon	Heptagon	Octagon
Bottom	0.0851	0.1305	0.1478	0.1253	0.1173	0.1375
	0.0478	0.0848	0.1245	0.0785	0.0722	0.0916
	0.0680	0.1140	0.1346	0.1085	0.0857	0.1265
Left	0.0664	0.3051	0.1129	0.1243	0.0686	0.1529
	0.0308	0.2352	0.0458	0.0859	0.0476	0.0907
	0.0589	0.2122	0.0555	0.0988	0.0773	0.0794
Right	0.0724	0.2265	0.0429	0.1050	0.050	0.1052
	0.0643	0.2918	0.0893	0.0847	0.0387	0.1098
	0.1046	0.3055	0.1164	0.1253	0.0637	0.1518
Top	0.0637	0.5625	0.1858	0.1269	0.1062	0.1439
	0.0680	0.5487	0.1730	0.1011	0.0848	0.1161
	0.0967	0.5182	0.1579	0.1342	0.0989	0.1332
Average	0.0689	0.2946	0.1155	0.1082	0.0759	0.1199

To draw further remarks regarding the central deposition geometry, the DTB method was employed to identify a more accurate representation of the 2.6 wt% weight ratio 1:4 deposition. As illustrated in Fig. 1(b), the method initially converts the top view of the deposition into a binary image and slices it into four different halves [55]. The profile in each half is extracted into a plot and subtracted against reference polygons to obtain ΔP. The ΔP for each half is then consolidated into the RSME and tabulated in Tables 1 and 2. In Table 2, each row of RSME (ΔP) across all halves corresponds to a single set of data obtained from one deposition. The DTB is a shape recognition method that is more accurate in determining the shape of a profile compared to the mathematical methods using circularity and roundness values. DTB method creates an overlapped quadrant between two halves, allowing us to firmly establish the geometry. For example, if the top and left profiles resemble a circular profile, the overlapping quadrant on the top-left corner can be resolved as a circular corner. Hence, the RSME (ΔP) must be low to show resemblance to any regular polygonal geometries. As the DTB method was modified to include an error value, we implemented a 90% confidence interval to establish a 10% RSME of ΔP threshold to claim the similarity of the outline to the reference polygon. Table 1 tabulated the reference polygons against the 2.6 wt% weight ratio 1:1 deposition. The average on the last row computes the average of RSME of ΔP in all halves. The RSME shows a 3% error for the visually octagonal deposition patterned against a reference octagon, validating the method practicability.

Based on the minimum RSME (ΔP) from Table 2, the plot profile represents a circular geometry on most occasions except on the right profile and one occasion on the left profile. The left profile shows signs of a heptagon, while the right profile consistently appears to be a heptagon in all events. The RSME average from three deposition patterns concludes the irregular outline of the 2.6 wt% weight 1:4 deposition formed in the liquid–air interface has the closest resemblance to a circular profile given the smallest error of about 6%. However, it also reflects a reasonably low RSME below 10% to a heptagon.

Revisiting Fig. 2, there is a consistent trend marked by the progressive augmentation of particle deposition at the droplet center, mirroring the increasing presence of the 10 μm particles. At the 3:1 weight ratio, an elevation in particle concentration corresponds to a surge in the 10 μm particle population within the suspension droplet, thereby accentuating the deposition at the drop center through gravitational sedimentation. Introducing a minute proportion of larger particles emerges as a strategic technique to optimize deposition, culminating in a more uniform configuration, as validated by the particle distribution showcased in Fig. 4. Upon transitioning to the weight ratios of 1:1 and 1:4, the propensity of aggregates to disperse away from the contact line further amplifies the central deposition. In essence, while the 3 μm particles exhibit interactions akin to their behavior within pure colloidal solutions, the introduction of a minor fraction of the 3 μm particles within a droplet laden with the 10 μm particles resulted in a significant transformation in the resultant dried pattern, primarily attributed to shifts in packing configurations.

4. Conclusion

The findings presented herein demonstrate the capacity of a mixture comprising 3 μm and 10 μm particles at varying weight ratios to address two pivotal inquiries inherent to evaporative-driven self-assembly in polygonal sessile droplets. Primarily, the study introduced a robust approach to mitigating the coffee-ring effect during deposition. Additionally, it unveiled a versatile printing methodology that empowers the controlled modulation of both particle deposition pattern and geometry through the judicious combination of the bi-particle size solutions across five compositions.

Each distinct deposition pattern had been succinctly encapsulated within a comprehensive phase diagram, effectively underscoring the interplay between bi-particle mixing ratios and particle concentration. At the low particle concentration of 0.1 wt%, the distinctive behaviors of the individual particle sizes manifest, owing to the minimal particle count. In the case of the 3 μm:10 μm particle mixture at the 3:1 weight ratio, an intriguing transition from an octagonal outer-ring pattern to a uniform octagonal configuration emerged as the particle concentration escalates from 0.5 wt% to 1.0 wt% and beyond. The transformation stemmed from the interaction between particles of differing sizes. Specifically, the aggregates of the 3 μm particles encompassing the 10 μm particles were precipitated, in conjunction with the 10 μm particles, towards the drop center due to the influence of gravitational sedimentation acting on the larger particles. The efficacy of the studied approach in diminishing the coffee-ring effect in deposition was attested through the utilization of a confocal microscope, which confirms the attainment of particle distribution uniformity.

Upon elevating the proportion of the 10 μm particles in the mixture to 50%, a particle size segregation phenomenon emerged, observed in the 10 μm particle aggregates encircling the three-phase contact line at intermediate particle concentrations of 0.5 wt% and 1.0 wt%. The particle size segregation effect resulted in the formation of an octagonal outer-ring with irregular bits pattern. Analogous deposition patterns were also identified in suspensions featuring a weight ratio of 1:4 at 0.5 wt%. Further elevation of particle concentration for weight ratio 1:1, reaching 2.6 wt%, led to the creation of a central deposition on an octagonal platform. Similarly, intensifying particle concentration for the weight ratio 1:4 at 1.0 wt% and beyond yields a central deposition. The latter was engendered by the combined influences of liquid–air interface adsorption and escalating buoyant forces acting upon the adsorbed aggregates. The presence of 3 μm particles facilitates close packing of the 10 μm particles, augmenting the rate of agglomeration and consequently inducing aggregate growth and their migration toward the drop apex. This progression, driven by increased buoyant force, ultimately results in the formation of a central deposition. It is also worth noting that the curvature effect is underscored as pivotal in controlling the outline of the deposition geometry.

Lastly, a discernible trend emerges where the increased concentration of 10 μm particles corresponds to an augmented particle distribution within the central region in terms of particle concentration and mixing ratio.

CRediT authorship contribution statement

Si Xian Lim: Writing – review & editing, Writing – original draft, Visualization, Validation, Methodology, Investigation, Formal analysis, Data curation, Conceptualization. **Alistair Guo Hao Teo:** Visualization, Validation, Investigation, Data curation. **Kian-Soo Ong:** Resources, Methodology. **Karen Siew Ling Chong:** Methodology, Resources. **Fei Duan:** Resources, Conceptualization, Funding acquisition, Methodology, Project administration, Supervision, Writing – original draft, Writing – review & editing.

Declaration of competing interest

The authors declare that they have no known competing financial interests or personal relationships that could have appeared to influence the work reported in this paper.

Data availability

Data will be made available on request.

Acknowledgments

The authors acknowledge the support of Singapore Center for 3D Printing (SC3DP) and School of Mechanical and Aerospace Engineering at Nanyang Technological University, Singapore.

Appendix A. Supplementary data

A supporting sideo (SV1) showing the flocculation process for the suspension droplets of weight ratio 1:4 at 1.0 wt% and 2.6 wt%.

Supplementary material related to this article can be found online at https://doi.org/10.1016/j.colsurfa.2024.133884.

References

[1] P. Verding, P. Pobedinskas, R.M. Joy, E. Ahmed, Z. Remes, R.S.N. Kumar, S. Baron, M. Höfer, V. Sittinger, M. Neslaádek, K. Haenen, W. Deferme, The influence of droplet-based seeding of nanodiamond particles on the morpohological, optical, and mechanical properties of diamond coatings on glass, Surf. Coat. Technol. 459 (2023) 129391, http://dx.doi.org/10.1016/j.surfcoat.2023.129391.

[2] R.S.N. Kumar, A.V. Ramirez, P. Verding, P. Nivelle, F. Renner, J. D'Haen, W. Deferme, Deposition of ultra-thin coatings by a nature inspired spray-on-screen technology, Commun. Eng. 2 (2023) 42, http://dx.doi.org/10.1038/s44172-023-00093-0.

[3] S. Lee, A.M. Tiara, G. Cho, J. Lee, Control of the drying patterns for complex colloidal solutions and their applicatios, Nanomaterials (Basel) 12 (2022) 2600, http://dx.doi.org/10.3390/nano12152600.

[4] H.H. Lee, S.C. Fu, C.Y. Tso, C.Y.H. Chao, Study of residue patterns of aqueous nanofluid droplets with different particle sizes and concentrations on different substrates, Int. J. Heat Mass Transfer 105 (2017) 230–236, http://dx.doi.org/10.1016/j.ijheatmasstransfer.2016.09.093.

[5] D. Lohani, M.G. Basavaraj, D.K. Satapathy, S. Sarkar, Coupled effect of concnetration, particle size and substrate morphology on the formation of coffee rings, Colloids Surf. A 589 (2020) 124387, http://dx.doi.org/10.1016/j.colsurfa.2019.124387.

[6] F. Du, L. Zhang, W. Shen, Controllable dried patterns of colloidal drops, J. Colloid Interface Sci. 606 (2022) 758–767, http://dx.doi.org/10.1016/j.jcis.2021.08.089.

[7] Y. Li, C. Lv, Z. Li, D. Quéré, Q. Zheng, From coffee rings to coffee eyes, Soft Matter 11 (2015) 4669–4673, http://dx.doi.org/10.1039/C5SM00654F.

[8] L.K. Malla, R. Bhardwaj, A. Neild, Colloidal deposit of an evaporating sessile droplet on a non-uniformly heated substrate, Colloids Surf. A 584 (2020) 124009, http://dx.doi.org/10.1016/j.colsurfa.2019.124009.

[9] D. Mampallil, J. Reboud, R. Wilson, D. Wylie, D.R. Klug, J.M. Cooper, Acoustic suppression of the coffee-ring effect, Soft Matter 11 (2015) 7207–7213, http://dx.doi.org/10.1039/C5SM01196E.

[10] P. Kabi, R. Pal, S. Basu, Moses effect: Splitting a sessile droplet using a vapor-mediated Marangoni effect leading to designer surface patterns, Langmuir 36 (2020) 1279–1287, http://dx.doi.org/10.1021/acs.langmuir.9b03690.

[11] T. Kajiya, W. Kobayashi, T. Okuzono, M. Doi, Controlling the drying and film formation processes of polymer solution droplets with addition of small amount of surfactants, J. Phys. Chem. B 113 (2009) 15460–15466, http://dx.doi.org/10.1021/jp9077757.

[12] V.X. Nguyen, K.J. Stebe, Patterning of small particles by a surfactant-enhanced Marangoni–Bénard instability, Phys. Rev. Lett. 88 (2002) 164501, http://dx.doi.org/10.1103/PhysRevLett.88.164501.

[13] T. Still, P.J. Yunker, A.G. Yodh, Surfactant-induced Marangoni eddies alter the coffee-rings of evaporating colloidal drops, Langmuir 28 (2012) 4984–4988, http://dx.doi.org/10.1021/la204928m.

[14] A. Shimoni, S. Azoubel, S. Magdassi, Inkjet printing of flexible high-performance carbon nanotube transparent conductive films by coffee-ring effect, Nanoscale 6 (2014) 1184–1189, http://dx.doi.org/10.1039/C4NR02133A.

[15] S. Chen, M. Su, C. Zhang, M. Gao, B. Bao, Q. Yang, B. Su, Y. Song, Fabrication of nanoscale circuits on inkjet-printing patterned substrates, Adv. Mater. 27 (2015) 3928–3933, http://dx.doi.org/10.1002/adma.201500225.

[16] L. Zhang, H. Liu, Y. Zhao, X. Sun, Y. Wen, Y. Guo, X. Gao, C. Di, G. Yu, Y. Liu, Inkjet printing high-resolution, large-area graphene patterns by coffee-ring lithography, Adv. Mater. (Weinheim) 24 (2012) 436–440, http://dx.doi.org/10.1002/adma.201103620.

[17] B.-J. de Gan, P.C. Duineveld, U.S. Schubert, Inkjet printing of polymers: state of the art and future developments, Adv. Mater. (Weinheim) 16 (2004) 203–213, http://dx.doi.org/10.1002/adma.200300385.

[18] P. Zhou, H. Yu, W. Zou, Z. Wang, L. Liu, High-resolution and controllable nanodeposition pattern of Ag nanoparticles by electrohydrodynamic jet printing combined with coffee ring effect, Adv. Mater. Interfaces 6 (2019) 900912, http://dx.doi.org/10.1002/admi.201900912.

[19] H. Li, Y. Duan, Z. Shao, G. Zhang, H. Li, Y. Huang, Z. Yin, High-resolution pixelated light emitting diodes based on electrohydrodynamic printing and coffee-ring-free quantum dot film, Adv. Mater. Technol. 5 (2020) 2000401, http://dx.doi.org/10.1002/admt.202000401.

[20] G. Zhang, H. Zhang, R. Yu, Y. Duan, Y. Huang, Z. Yin, Critical size/viscosity for coffee-ring-free printing of perovskite micro/nanopatterns, ACS Appl. Mater. Interfaces 14 (2022) 14712–14720, http://dx.doi.org/10.1021/acsami.1c23630.

[21] M.J. Schertzer, M.J. Ahamed, R. Ben-Mrad, P. Lea, P.E. Sullivan, Characterizing the surface quality and droplet interface shape for microarray plates, Langmuir 28 (2012) 9961–9966, http://dx.doi.org/10.1021/la302091t.

[22] S. Luo, Z. Chen, Z. Dong, Y. Fan, Y. Chen, B. Liu, C. Yu, C. Li, H. Dai, H. Li, Uniform spread of high-speed drops on superhydrophobic surface by live-oligomeric surfactant jamming, Adv. Mater. 31 (2019) 904475, http://dx.doi.org/10.1002/adma.201904475.

[23] X. Zhang, C. Gong, O.U. Akakuru, Z. Su, A. Wu, G. Wei, The design and biomedical applications of self-assembled two-dimensional organic biomaterials, Chem. Soc. Rev. 48 (2019) 5564–5595, http://dx.doi.org/10.1039/C8CS01003J.

[24] V. Ferrara, G. Zito, G. Arrabito, S. Cataldo, M. Scopelliti, C. Giordano, V. Vetri, B. Pignataro, Aqueous processed biopolymer interfaces for single-cell microarrays, ACS Biomater. Sci. Eng. 6 (2020) 3174–3186, http://dx.doi.org/10.1021/acsbiomaterials.9b01871.

[25] S.-W. Wang, H.-Y. Lin, C.-C. Lin, T.S. Kao, K.-J. Chen, H.-V. Han, J.-R. Li, P.-T. Lee, H.-M. Chen, M.-H. Hong, Pulsed-laser micropatterned quantum-dot array for white light source, Sci. Rep. 6 (2016) 23563, http://dx.doi.org/10.1038/srep23563.

[26] L. Ammosova, Y. Jiang, M. Suvanto, T.A. Pakkanen, Precise micropatterning of silver nanoparticles on plastic substrates, Appl. Surf. Sci. 401 (2017) 353–361, http://dx.doi.org/10.1016/j.apsusc.2017.01.018.

[27] T. Xu, L.-P. Xu, X. Zhang, S. Wang, Bioinspired superwettable micropatterns for biosensing, Chem. Soc. Rev. 48 (2019) 3153–3165, http://dx.doi.org/10.1039/C8CS00915E.

[28] J.T. Wen, C.M. Ho, P.B. Lillehoj, Coffee ring aptasensor for rapid protein detection, Langmuir 29 (2013) 8440–8446, http://dx.doi.org/10.1021/la400224a.

[29] J.B. Lee, H.R. Gwon, S.H. Lee, M. Cho, Wetting transition characteristics on microstructured hydrophobic surfaces, Mater. Trans. 51 (2010) 1709–1711, http://dx.doi.org/10.2320/matertrans.M2010118.

[30] D. Rawtani, Y.K. Agrawal, Emerging strategies and applications of layer-by-layer self-assembly, Nanobiomedicine 1 (2014) 8, http://dx.doi.org/10.5772/600.

[31] H. Kim, F. Boulogne, E. Um, I. Jacobi, E. Button, H.A. Stone, Controlled uniform coating from the interplay of Marangoni flows and surface adsorbed macromolecules, Phys. Rev. Lett. 116 (2016) 124501, http://dx.doi.org/10.1103/PhysRevLett.116.124501.

[32] J. Park, J. Moon, Contorl of colloidal particle deposit patterns within picoliter droplets ejected by ink-jet printing, Langmuir 22 (2006) 3506–3513, http://dx.doi.org/10.1021/la053450j.

[33] R. Deleurence, C. Parneix, C. Monteux, Mixtures of latex particles and the surfactant of opposite charge used as interface stabilizers–influence of particle contact angle, zeta potential, flocculation and shear energy, Soft Matter 10 (2014) 7088–7095, http://dx.doi.org/10.1039/C4SM00237G.

[34] R. Bhardwaj, X. Fang, P. Somasundaran, D. Attinger, Self-assembly of colloidal particles from evaporating droplets: Role of DLVO interactions and proposition of a phase diagram, Langmuir 26 (2010) 7833–7842, http://dx.doi.org/10.1021/la9047227.

[35] L.K. Malla, R. Bhardwaj, A. Neild, Analysis of profile and morphology of colloidal deposits obtained from evaporating sessile droplets, Colloids Surf. A 567 (2019) 150–160, http://dx.doi.org/10.1016/j.colsurfa.2019.01.028.

[36] H. Zargartalebi, S.H. Hejazi, A. Sanati-Nezhad, Self-assembly of hihgly ordered micro- and nanoparticle deposits, Nat. Commun. 13 (2022) 3085, http://dx.doi.org/10.1038/s41467-022-30660-6.

[37] D. Zhang, J. Fang, T. Li, Sensitive and uniform detection using surface-enhanced Raman scattering: Influence of colloidal-droplets evaporation based on Au-Ag alloy nanourchins, J. Colloid Interface Sci. 514 (2018) 17–226, http://dx.doi.org/10.1016/j.jcis.2017.12.017.

[38] J. Xu, J. Du, C. Jing, Y. Zhang, J. Cui, Facile detection of polycyclic aromatic hydrocarbons by a surface-enhanced Raman scattering sensor based on the Au coffee ring effect, ACS Appl. Mater. Interfaces 6 (2014) 6891–6897, http://dx.doi.org/10.1021/am500705a.

[39] W. Wang, Y. Yin, Z. Tan, J. Liu, Coffee-ring effect-based simultaneous SERs substrate fabrication and analyte enrichment for trace analysis, Nanoscale 6 (2014) 9588–9593, http://dx.doi.org/10.1039/C4NR03198A.

[40] I. Barman, N.C. Dingari, J.W. Kang, G.L. Horowitz, R.R. Dasari, M.S. Feld, Raman spectroscopy-based sensitive and specific detection of glycated hemoglobin, Anal. Chem. 84 (2012) 2474–2482, http://dx.doi.org/10.1021/ac203266a.

[41] R. Que, M. Shao, S. Zhuo, C. Wen, S. Wang, S.-T. Lee, Highly reproducible surface-enhanced raman scattering on a capillarity-assisted gold nanoparticle assembly, Adv. Funct. Mater. 21 (2011) 3337–3343, http://dx.doi.org/10.1002/adfm.201100641.

[42] F. Qi, Z. Meng, M. Xue, L. Qiu, Recent advances in self-assemblies and sensing applications of colloidal photonic crystals, Anal. Chim. Acta 1123 (2020) 91–112, http://dx.doi.org/10.1016/j.aca.2020.02.026.

[43] R.J. Vrancken, M.K. Blow, H. Ksumaatmaja, K. Hermans, A.M. Prenen, C.W.M. Bastiaansen, D.J. Broer, J.M. Yeomans, Anisotropic wetting and de-wetting of drops on substrates patterned with polygonal post, Soft Matter 9 (2013) 674, http://dx.doi.org/10.1039/C2SM26393A.

[44] R. Raj, S. Adera, R. Enright, E.N. Wang, High-resolutoin liquid patterns via three-dimensional droplet shape control, Nat. Commun. 5 (2014) 4975, http://dx.doi.org/10.1038/ncomms5975.

[45] V. Kubyshikina, D. Orejon, C.M. Dover, K. Sefiane, Geometrical deposits on microstructured surfaces, J. Bionic Eng. 17 (2020) 851–865, http://dx.doi.org/10.1007/s42235-020-0071-y.

[46] R. Iqbal, B. Majhy, A.Q. Shen, A.K. Sen, Evaproation and morphological patterns of bi-dispersed colloidal droplets on hydrophilic and hydrophobic surfaces, Soft Matter 14 (2018) 9901, http://dx.doi.org/10.1039/C8SM01915K.

[47] H.K. Park, Y. Kim, H. Min, C. Pang, B.M. Weon, Hexagonal deposits of colloidal particles, Phys. Rev. Let. E 100 (2019) 022602, http://dx.doi.org/10.1103/PhysRevE.100.022602.

[48] H. Kim, M. Gonçalves, S.H. Kang, B.M. Weon, High density deposits of binary colloids, Sci. Rep. 12 (2022) 22307, http://dx.doi.org/10.1038/s41598-022-26151-9.

[49] J. Pyeon, K.M. Song, Y.S. Jung, H. Kim, Self-induced solutal Marangoni flows realize coffee-ring less quantum dot microarrays with extensive geometric tunability and scability, Adv. Sci. 9 (2022) 2104519, http://dx.doi.org/10.1002/advs.202104519.

[50] J. Merrin, S. Leibler, J.S. Chuang, Printing multistrain bacterial patterns with a piezoelectric inkjet printer, PLoS One 2 (2007) e663, http://dx.doi.org/10.1371/journal.pone.0000663.

[51] S. Gupta, M.R. Thombare, N.D. Patil, Pinning and depinning dynamics of an evaporating sessile droplet containing mono- and bidispersed colloidal particles on a nonheated/heated hydrophobic substrate, Langmuir 39 (2023) 3102–3117, http://dx.doi.org/10.1021/acs.langmuir.2c03270.

[52] M.D. Shafiq, F. Waggett, E. Norris, P. Bartlett, Droplet evaporation: Colloidal interactions vs. evaporation kinetics, Colloids Surf. A 578 (2019) 123555, http://dx.doi.org/10.1016/j.colsurfa.2019.06.020.

[53] N.D. Patil, R. Bhardwaj, A. Sharma, Self-sorting of bidispersed colloidal particles near contact line of an evaporating sessile droplet, Langmuir 34 (2018) 12058–12070, http://dx.doi.org/10.1021/acs.langmuir.8b00427.

[54] S.X. Lim, J. Ren, K.-S. Ong, K.S.L. Chong, F. Duan, Evaporation-driven octagonal particle deposition on the patterned substrate, Droplet 1 (2022) 202–213, http://dx.doi.org/10.1002/dro2.30.

[55] F. Qin, B. Fang, H. Zhao, Traffic sign segmentation and recognition in scene images, in: 2010 Chinese Conference on Pattern Recognition, CCPR, 2010, pp. 1–5, http://dx.doi.org/10.1109/CCPR.2010.5659271.

[56] L. Bansal, P. Seth, B. Murugappan, S. Basu, Suppression of coffee ring: (particle) size matters, Appl. Phys. Lett. 112 (2018) 211605, http://dx.doi.org/10.1063/1.5034119.

[57] B.M. Weon, J.H. Je, Capillary force repels coffee-ring effect, Phys. Rev. E 82 (2010) 015305, http://dx.doi.org/10.1103/PhysRevE.82.015305.

[58] P. Rangamani, R. Iyengar, Modelling spatio-temporal interactions within the cell, J. Biosci. 32 (2007) 157–167, http://dx.doi.org/10.1007/s12038-007-0014-3.

[59] D. Chicea, Coherent light scattering on nanofluids: Computer simulation results, Appl. Opt. 47 (2008) 1434–1442, http://dx.doi.org/10.1364/AO.47.001434.

[60] M. Matsuzaki, H. Kikura, J. Matsushita, M. Aritomi, H. Akatsuka, Real-time observation of Brownian motion and cluster movement of ferro- and non-magnetic particles in mnagenetic field, Sci. Technol. Adv. Mater. 5 (2004) 667–671, http://dx.doi.org/10.1016/j.stam.2004.03.012.

[61] J. Shang, M. Flury, Y. Deng, Force measurements between particles and the air–water interface: Implications for particle mobilization in unsaturated porous media, Water Resour. Res. 45 (2009) W06420, http://dx.doi.org/10.1029/2008WR007384.